ANNUAL REVIEWS

First-Principles Insights into Plasmon-Induced Catalysis

John Mark P. Martirez,[1] Junwei Lucas Bao,[2]
and Emily A. Carter[1,2,3]

[1] Department of Chemical and Biomolecular Engineering, University of California, Los Angeles, Los Angeles, California 90095, USA; email: eac@ucla.edu

[2] Department of Mechanical and Aerospace Engineering, Princeton University, Princeton, New Jersey 08544, USA

[3] Office of the Chancellor, University of California, Los Angeles, Los Angeles, California 90095, USA

ANNUAL REVIEWS CONNECT

www.annualreviews.org

- Download figures
- Navigate cited references
- Keyword search
- Explore related articles
- Share via email or social media

Keywords

plasmonic catalysis, correlated wavefunction methods, density functional theory, heterogeneous catalysis, photocatalysis, embedding methods

Abstract

The size- and shape-controlled enhanced optical response of metal nanoparticles (NPs) is referred to as a localized surface plasmon resonance (LSPR). LSPRs result in amplified surface and interparticle electric fields, which then enhance light absorption of the molecules or other materials coupled to the metallic NPs and/or generate hot carriers within the NPs themselves. When mediated by metallic NPs, photocatalysis can take advantage of this unique optical phenomenon. This review highlights the contributions of quantum mechanical modeling in understanding and guiding current attempts to incorporate plasmonic excitations to improve the kinetics of heterogeneously catalyzed reactions. A range of first-principles quantum mechanics techniques has offered insights, from ground-state density functional theory (DFT) to excited-state theories such as multireference correlated wavefunction methods. Here we discuss the advantages and limitations of these methods in the context of accurately capturing plasmonic effects, with accompanying examples.

1. INTRODUCTION

1.1. The Nature of Plasmons and Localized Surface Plasmon Resonances

Metals scatter light by screening the electric field of an incident light wave. If the frequency of the light is below a certain threshold (plasma frequency, ω_P), the metal's nearly free electrons oscillate opposite to the direction of the light's electric field, with the light then reflected (with some absorbed), giving metals a metallic sheen. When metal particles are smaller than the wavelength of incident photons, the particles experience a uniform electric field at an instant in time. The nearly free electrons of the metal nanoparticles (NPs) then oscillate collectively with the same frequency as the incident light and are said to be in resonance (**Figure 1a**). For example, metal NPs with diameters between ~10 and ~100 nm have a strong optical response to ultraviolet (UV) and visible (Vis) light, which have wavelengths of a few hundreds of nanometers. This special light–matter interaction at the nanoscale is referred to as a localized surface plasmon resonance (LSPR).

The peak LSPR extinction frequency (ω_{SP}) of a metal NP depends on the metal's ω_P, the dielectric properties of the surrounding medium, and the size and geometry of the NP (1, 2). For nanosized spheres of Al (e.g., diameter, $d = 70$–220 nm), ω_{SP} is within the Vis to deep UV (3); for Au spherical NPs (e.g., $d = 9$–99 nm), ω_{SP} lies between orange and blue in the Vis (4), while ω_{SP} of hexagonal nanoplatelets of Mg (e.g., $d = 100$–300 nm, 30–60 nm thick) ranges from near-infrared (NIR) to UV (5). Metals with nearly free electron–like valence electronic structure exhibit the strongest LSPR responses, with large negative real and small imaginary (related to resonance broadening and dissipation) optical dielectric functions (2). Distinguishing light scattering from absorption, referred to collectively as extinction, is important in plasmonics. High-light-scattering (absorbing) metals tend to exhibit strong (damped) LSPRs. A high-quality plasmonic response
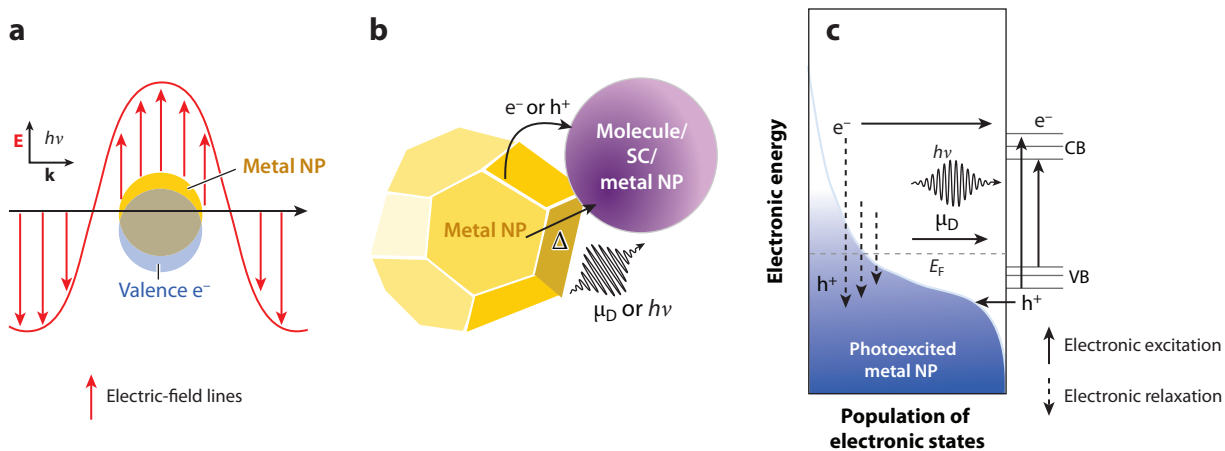
Figure 1

(*a*) An illustration of the collective oscillation of the valence electrons (e⁻) of a metal nanoparticle (NP) in response to the oscillating electric field (**E**) of an incident light wave propagating along **k**. (*b*) A diagram depicting possible energy transfer mechanisms between a plasmonic metal NP and a molecule, semiconductor (SC), or metal NP. These mechanisms are hot-carrier injection (e⁻ or hole, h⁺), photothermal heating (Δ), and direct excitation via far-field (light reemission, *hν*) or near-field (resonance energy transfer via dipole-field interaction, μ_D) interaction. (*c, left*) A schematic representation of the thermalized electron population of states in a metal near the Fermi level, E_F, at finite temperatures, following a localized surface plasmon resonance (LSPR) excitation (*blue shaded curve*). (*Right*) Interfacial, defect-, or adsorbate-induced local surface states are represented: valence band (VB) for SCs or highest-occupied molecular orbital (HOMO) for molecules and conduction band (CB) for SCs or lowest-unoccupied molecular orbital (LUMO) for molecules. For a coupled metal, these states would be a continuum. The LSPR may induce an excitation within these states either radiatively or via a near-field resonance energy transfer. Finally, direct electron transfer is also illustrated.

emerges from alkali and coinage metals (Cu, Ag, and Au) as well as from aluminum, whereas transition metals with partially occupied *d* bands absorb across intraband transitions, dampening their plasmonic response. Therefore, the latter are aptly referred to as lossy. A combination of plasmonic and lossy metals, via either doping or particle coupling, can diversify the optoelectronic properties and chemical reactivity of metal NPs (Section 1.3).

1.2. Experimental Demonstration of Plasmon-Driven Catalysis

The LSPR's influence in chemistry began with the discovery of surface-enhanced Raman spectroscopy (6, 7). This pronounced optical response in which metal NPs act as amplifiers of both the incoming and outgoing light wave created new subfields and inspired applications, including, recently, heterogeneous photocatalysis. The field of plasmonic catalysis also has exploded, with over 5,000 papers published on the topic in the last 10 years (8). Demonstrations of the power of plasmonic catalysis involved accelerating simple to complex reactions that occur slowly in the dark at room temperature. Reactions such as room temperature dissociation and desorption of hydrogen (H_2) on Au (9, 10) and Al (11) NPs, ethylene epoxidation with oxygen (O_2) on Ag NPs at mild temperatures (12), carbon dioxide (CO_2) reduction with H_2 to carbon monoxide (CO) and methane (CH_4) on Rh nanocubes and Au spherical NPs (13), organic Sonogashira and Hiyama cross-coupling reactions on Au-Pd NP alloys (14), and CO_2 reduction to ethane (C_2H_6) on spherical Au NPs (15) are enhanced upon illumination, with a characteristic maximum activity at or near the ω_{SP} of the NPs. More examples are provided below and are discussed in the context of novel plasmonic NP architectures (Section 1.3) and the computational methods used to understand the role of plasmonics in their catalysis (Sections 3 and 4).

1.3. Advances in Plasmonic Architectures

Advances in synthesis, e.g., via solvent and precursor selection, enable the precise control of the size and shape of metal NPs (16) and the construction of exotic architectures (17–19) that can produce diverse optoelectronic properties. However, only a few metals exhibit high-quality LSPRs within the UV-Vis spectrum, and although those can catalyze certain reactions, plasmonic enhancement of a wider array of reactions could be groundbreaking. An obvious approach is to prepare surface-doped or -alloyed metal NPs. Doped or alloyed NPs of Au with Fe (20, 21), Zn (22), or Pd (14, 23) and of Cu with Ru (24–26) were synthesized and their plasmonic response characterized. Although this strategy seems straightforward, it faces a diverse set of challenges, from synthesis (not all elements form alloys easily) to control of optoelectronic properties (even at low concentrations, i.e., with doping, lossy metals can diminish the plasmonic response of the host metal). For a comprehensive review of nanoalloy synthesis, characterization, and applications, see Reference 16. Another coupling strategy, especially for immiscible metals, is to separate components for light scattering and absorption and for catalysis, thus building heterostructures. In such so-called antenna–reactor structures (27), the plasmonic metal antenna either enhances light absorption by the coupled reactor metal or serves as a source of hot carriers injected into the latter. Three such configurations exist: core-shell (28, 29), tandem (27, 30, 31), and surface-decorated (32–34) structures. Core-shell structures, as the name implies, refer to plasmonic NPs wrapped by a secondary material, e.g., an Ag nanocube with a Pt skin (28). Tandem structures consist of NP spheres, rods, or disks, and dumbbell structures in which plasmonic rods are capped by a secondary material at the ends. So-called nanodumbbells composed of Au nanorods with Pd end-caps have enabled the plasmon-driven catalytic dehydrogenation of formic acid (30) and Suzuki coupling reactions (31). Surface decoration pertains to smaller reactor particles scattered on the surface

of plasmonic NPs. Swearer et al. (32), for example, synthesized Al NPs decorated with different transition metal clusters, or nanoislands. For a review of the synthesis and plasmonic properties of hybrid or multifunctional metal NPs, see Reference 35.

2. MECHANISMS OF PLASMONIC ENHANCEMENT OF CATALYSIS

Referred to as Landau damping, LSPR decay is the result of the dephasing of the collective valence electron oscillations. As in any electronic transition, LSPR damping can be characterized by a multitude of processes occurring at different timescales. These LSPR relaxation modes are discussed in detail in recent reviews (36–39). **Figure 1b** highlights the three primary energy transfer modes relevant to photocatalysis.

2.1. Hot-Carrier Generation and Injection

Energetic charge-carrier injection (hot electrons or holes) into an adsorbed molecule on metal NPs is one primary mechanism of plasmon-induced photochemical reactions (37, 40). A transient ion state forms that is intrinsically less stable and thus reacts more readily (12, 42). This mechanism implies that charge transfer (CT) occurs from the metal to the adsorbate or vice versa. Electron–electron scattering thermalizes the hot carriers, yielding a broad electronic energy distribution (43) potentially available for CT catalysis. Carrier injection into the coupled molecule or material requires empty state(s) at or below the metal NP's Fermi level$+\hbar\omega_{\mathrm{SP}}$, and occupied state(s) at or above the metal NP's Fermi level$-\hbar\omega_{\mathrm{SP}}$ (**Figure 1c**). This assumes an equitable energy distribution between the two excited carriers, e.g., as in Al and Ag (44). Strong participation of the fully filled d orbitals in hot-carrier generation (interband transition from d to valence s), e.g., in Cu and Au, gives rise to higher-energy excited holes and lower-energy excited electrons, i.e., holes that are hotter than electrons (44). Interfacial resistance (a Schottky barrier) also controls carrier injection efficiency (45). The role of electron transitions aiding desorption of molecules off metallic surfaces is not new. Desorption induced by electronic transitions (46) and by multiple electronic transitions (47) has been studied experimentally and theoretically as a model for nonadiabatic surface dynamics on metallic surfaces for more than half a century (46, 48, 49). Plasmonic catalysis, however, invokes CT to catalyze surface reactions beyond adsorbate desorption, i.e., molecular bond breaking. The experimental or theoretical characterization of adsorbate frontier states and their energies relative to the metal's Fermi level provides clues regarding whether CT can be used to catalyze the surface reaction. However, the use of ground electronic states derived from, e.g., density functional theory (DFT) for such analysis is questionable (Section 3.2).

2.2. Photothermal Heating

Electron–phonon coupling, occurring on the timescale of atomic vibrations, could be a viable means to catalyze reactions if carrier injection (Section 2.1) is impeded or electronic transitions within the reactor are significantly off-resonance with ω_{SP} (Section 2.3). This coupling also thermalizes the excited carriers, which lose energy in the form of heat (37). Light-induced local (photothermal) heating can increase the reactor temperature in the absence of other optical relaxation processes (50). A large photoinduced temperature swing can drive slow reactions without external heating (51). This mode of enhancement therefore does not differ from thermal catalysis, which ground-state quantum or even classical simulations can describe (Section 3.1).

2.3. Direct Surface Excitation via Far-Field (Light Emission) and Near-Field (Resonance Energy Transfer) Interactions

Plasmons can reemit photons as an avenue for LSPR relaxation. Chemical species that are more than a full wavelength away from the NP interact with scattered light in the usual way. However, species that are less than a wavelength away from the NPs do not experience a full light wave and therefore interact instead with a virtual photon. These interactions are referred to as far-field and near-field interactions, respectively (**Figure 1***c*).

Cushing et al. (52) used transient absorption and action spectroscopy to demonstrate coupling between the LSPR of a plasmonic metal and an adjacent SC through a radiationless near-field dipole–dipole interaction via a resonance energy transfer (RET) mechanism [Förster resonance energy transfer (FRET)]. The researchers aptly coined the term plasmon-induced resonance energy transfer (PI-RET) for this phenomenon (52). Hsu et al. (53) derived an expression for FRET between a donor and acceptor molecule mediated by a plasmonic NP, which the researchers called plasmon-coupled RET (PC-RET). In traditional FRET, the overlap between the donor emission and acceptor absorption spectra dictates the transfer rate, which diminishes with the donor–acceptor distance to the sixth power. In PI-RET, the plasmonic NP is the donor and the SC the acceptor. In PC-RET, the plasmonic NP acts as both donor and acceptor, a medium which amplifies the incoming (from the donor molecule) and outgoing (to the acceptor molecule) light wave. In both PI-RET and PC-RET, the researchers used the original FRET expression to rederive RET rates suitable for each case (52, 53). Martirez & Carter (54) extended these models to any acceptor molecule adsorbed on the surface of a metal NP. The Martirez-Carter model differs from that of Cushing et al. (52) in that the acceptor is a molecule with discrete states rather than bands as in an SC; it differs from the model of Hsu et al. (53) by the absence of a donor molecule. Martirez and Carter derived a molecular PI-RET rate that depends on the oscillator strength (f) of the electronic transitions of the adsorbate and the spectral overlap of these transitions with that of the metal NP's LSPR. Excited-state simulations can predict the absorption frequencies of the adsorbate molecule relevant to the reaction as well as their respective f values (Section 4). The explicit quantum mechanical treatment of the surface and the molecule includes the electronic coupling between the donor (metal) and the acceptor (molecule), which is ignored in FRET (55).

2.4. Can First-Principles Quantum Mechanics Simulations Capture These Mechanisms?

The mechanism of catalytic enhancement due to LSPRs can be explained by any of the physical phenomena previously described, and it is not always apparent which of them dominates. Measured rate enhancements suggesting decreased effective activation barriers point to the possibility of plasmon-enabled access to lower-barrier, electronically excited–state surfaces (13, 14, 24, 25, 56) via CT or RET (57). Multiple excitation events (CT or RET) may be required to complete a reaction. A superlinear dependence of the reaction rate on light intensity or power is an indicator of such phenomena (27, 58, 59). Measuring local temperatures at or near the illuminated area of the catalyst and performing Arrhenius analysis could differentiate electronic (CT or RET) from vibrational (photothermal) excitation (24–26, 33, 59). In the latter case, rate enhancements are due to local heating and should not alter the effective activation energy. First-principles quantum mechanical methods (Sections 3 and 4) can address the feasibility of each process. However, capturing all relevant physics is difficult due to either inherent methodological approximations or simulation size and timescale limitations. One can exploit the seeming short-sightedness of chemical reactions with respect to environmental influence on mechanisms and energetics. In other words,

simulations can focus on the reactor components of these hybrid structures or even only on the reactive site. Moreover, within this approximation, the oscillation of the electron density itself need not be simulated concurrently but just the consequences of the plasmon decay. In Sections 3 and 4, we discuss several quantum mechanics methods and the ground- and excited-state electronic and atomic features that may be extracted from them, which can explain or predict the role of plasmonics in heterogeneous catalysis.

3. THE THERMODYNAMICS AND KINETICS OF PLASMONIC CATALYSIS FROM DENSITY FUNCTIONAL THEORY

DFT within the Born-Oppenheimer approximation is a powerful quantum mechanical method that can be used to describe chemical systems at the atomic scale and is widely used to predict ground-state chemical reaction energetics and pathways. The Kohn-Sham approximation of DFT introduces one-electron orbitals in Slater determinants that often resemble intuitive molecular orbitals. These single-electron orbitals (and their energies) are often interpreted to carry meaning and are widely used to explain the chemistry and the ground- and even excited-state electronic properties of chemical species [band gaps, highest-occupied molecular orbital (HOMO) and lowest-unoccupied molecular orbital (LUMO) gaps, ionization energies, etc.], although their direct correspondence to physical observables is unfounded (60). Moreover, DFT electron exchange–correlation (XC) functionals inadequately describe CT and excited-state processes, which are important for (photo)electrochemical reactions, due to self-interaction error and the lack of a derivative discontinuity in the XC energy (61). XC functionals include, but are not limited to, the local density approximation (62) and the generalized gradient approximation (GGA) (63). Both forms use the electron density as input to evaluate the XC energy, while the latter also uses the gradient of the electron density. For the latter, the most cited form is the Perdew-Burke-Ernzerhof (PBE) approximation (63). A variant of PBE-GGA often employed to simulate heterogeneous catalysis is Hammer et al.'s (64) revised PBE, as it improves predicted molecular adsorption energies. Van der Waals corrections (65–70) [originating from mutually induced dipoles corresponding to simultaneous pairs of single electronic excitations, which are not captured by DFT with an approximate XC functional (71)] can be incorporated as well. Grimme and coworkers' (68) D method [e.g., D3 with Becke-Johnson damping (D3BJ) (65, 69)] gained prominence due to its straightforward form, requiring only nuclear coordinates as input and with dispersion coefficients for most elements precomputed and damping functions for popular XCs preparameterized (68, 69).

The determination of reaction energy landscapes using DFT is commonplace. From the point of view of heterogeneous catalysis, simulations are typically performed on the most stable surface facet(s), as these are seen as the most representative of the facets present on NPs. By examining catalysis on one facet at a time, one can take advantage of periodic boundary conditions to reduce the problem to that of characterizing chemistry in a periodically replicated unit cell. Within periodic boundary DFT, the most common technique for finding a minimum energy path (MEP) connecting two stationary structures and the corresponding transition state is the nudged elastic band (NEB) method (72). The climbing-image NEB (CI-NEB) offers a refined transition-state search by defining a structure able to climb along the MEP to the saddle point (73).

3.1. Ground-State Reaction Potential Energy Surfaces

In the context of plasmonic catalysis, potential energy surfaces (PESs) must be constructed for surface reactions on both ground and excited electronic states. DFT with CI-NEB can establish

ground-state MEPs; whether such pathways are relevant for the illuminated state of the catalyst depends on the nature of the reaction. Ground-state MEPs are not entirely irrelevant. For example, in the isotope exchange experiments mixing H_2 and D_2 to produce hydrogen deuteride (HD) on Au NPs (9) and Al-Pd antenna–reactor NPs (27), one can ascertain from DFT PESs that the plasmon-induced enhancement operates on dissociation and associative desorption of the molecule on Au and on Al-Pd, respectively, as these are the NPs' rate-limiting steps in the ground state. In the latter case, H_2 dissociation on Pd(111) in the ground state is virtually barrierless and extremely favorable, likely leading to saturation of the surface with H (27). Further, increased HD formation upon illumination (27) indicates that the Pd surface saturates less due to plasmon-driven H_2 desorption, which in turn enables more selective catalytic hydrogenation of acetylene to ethy-lene [and inhibits full hydrogenation to ethane (27)]. DFT-derived energetics can also identify rel-evant slow elementary steps in more complex reactions, for which additional electronic characteri-zation can be made or simulations further refined. For example, the decomposition of nitrous oxide $(N_2O)(g)$ to nitrogen $(N_2)(g)$ and $O_2(g)$ may proceed via many pathways. The particular bottleneck step(s) depends on the catalyst's ability to stabilize adsorbed reactants, intermediates, and products, namely, N_2O, O, N_2, and O_2. By investigating the thermodynamics of O, O_2, and N_2O adsorption on Ir(111) via DFT(GGA)+D3BJ, Swearer et al. (33) concluded that O_2 desorption is rate-limiting on Al-Ir antenna–reactor NPs due to the strength of O-Ir binding. The researchers further pre-dicted that a second N_2O molecule mediates the formation of adsorbed O_2 on Ir: $N_2O(g) + O(ad) \rightarrow O_2(ad) + N_2(g)$. The adsorbed O_2, a peroxide, faces a relatively large barrier to desorb, which is admittedly more surmountable than is that for the coupling of two O(ad) to O_2(ad). Experimentally, plasmon-driven N_2O decomposition on Al-Ir antenna–reactors is primarily photothermally activated (Section 2.2) and is autocatalyzed (33). The autocatalytic nature of the reaction originates from the very exoergic predicted preequilibrium step (N_2–O bond dissocia-tion) ($\Delta H = -2.45$ eV, $\Delta G = -1.55$ eV at 327°C) that drives the kinetically hindered endoergic O_2 desorption (33).

3.2. The Alignment of Adsorbate and Surface Frontier States as a Vehicle to Explain Possible Charge Transfer

Densities of states (DOSs) and projected DOSs (pDOSs) are often used to examine the nature of frontier electronic states. One can map out which orbital types, i.e., angular momenta and bonding nature (bonding, antibonding, or nonbonding), are occupied or empty, and which atoms contribute to these orbitals, thus providing chemically intuitive rationalizations of adsorption strengths and preferred adsorption geometries. In a pDOS, atomic orbitals of the constituent atoms typically are used to project their respective contributions to the total DOS, which can be resolved according to angular momenta (s, p, d, etc.). Bonding characters are not always apparent in such projections. A more sophisticated way to perform the projections is by using molecular orbitals formed by a pair of atoms, which are either bonding or antibonding. The crystal orbital Hamilton population (COHP) method constructs a library of orbitals and their pairings to perform the projection, thereby identifying bonding and antibonding contributions between pairs of atoms in the total DOS in a more automated way (74). The potential for adsorbate-surface CT (Section 2.1) thus can be determined at least qualitatively from pDOSs or COHPs and their energies. What follows are insights that result from such analyses.

Because no barrier exists to dissociate H_2 on Pd(111) (see Section 3.1), the more consequential process for Pd is believed to be the interaction of the generated hot carriers with adsorbed H and D atoms on Pd, inducing desorption of HD (27). To qualitatively investigate the relative influence
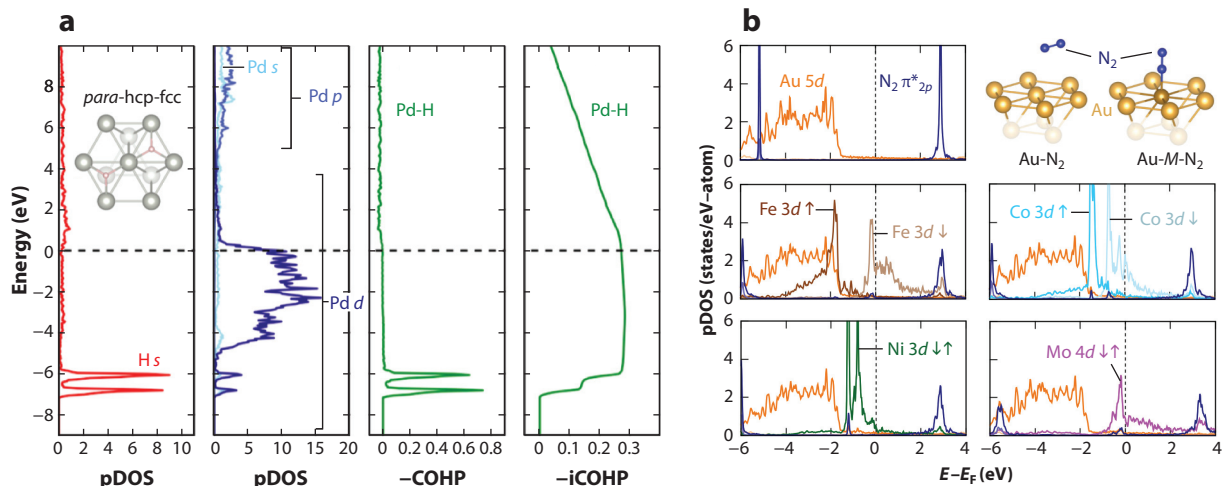
Figure 2

(*a*, *left* to *right*) These four graphs show, respectively, pDOS projected onto the valence orbitals of H and Pd, and the averaged −COHP and −iCOHP obtained from the projection of the Pd–H bonding and antibonding molecular orbitals onto the full-system DFT-PBE one-electron orbitals of the *para*-hcp-fcc structure (see inset in leftmost panel). The COHP was averaged over all six Pd–H bonds. Energies are referenced to the Fermi level (E_F). Panel *a* adapted from Reference 27; copyright 2016 National Academy of Sciences. (*b*) Illustrations showing pDOS for end-on adsorbed N_2 on pure and *M*-doped Au(111). The graphs show pDOS of the $2p$ states of N_2 (*dark blue*), spin-resolved frontier *d* states of *M* (Fe, *brown*; Co, *light blue*; Ni, *green*; and Mo, *purple*; *dark* and *light hues* for spin up and down, respectively, for Fe and Co), and $5d$ states of the nine nearest Au neighbors of *M* (*orange*). Energies are relative to E_F. Panel *b* adapted with permission from Reference 75; copyright 2016 American Chemical Society. Abbreviations: COHP, crystal orbital Hamilton population; DFT, density functional theory; fcc, face-centered cubic; hcp, hexagonal close-packed; iCOHP, integrated COHP; PBE, Perdew-Burke-Ernzerhof approximation; pDOS, projected densities of states.

of hot electrons versus hot holes on desorption, Swearer et al. (27) calculated the DOS and analyzed the contributions of Pd–H bonding and antibonding interactions from DFT(PBE)+D3BJ. For two H atoms adsorbed on the hexagonal close-packed (hcp) and face-centered cubic (fcc) hollow sites of Pd(111), the bonding Pd–H orbitals (−COHP) lie far below the Fermi level (by ~6 eV) so that a hot-hole-initiated process is prohibitively energy demanding (**Figure 2*a***). However, the Pd–H antibonding interactions (+COHP) lie just above the Fermi level and thus hot electrons are more likely to induce these interactions (**Figure 2*a***). These DFT predictions thus specify that the hot-electron-initiated destabilization of Pd–H bonds leading to desorption is probable.

While considering plasmonically enhanced N_2 dissociation, Martirez & Carter (75) found that vertically oriented N_2 physisorbed on top of Fe, Co, Ni, or Mo dopants in Au(111) has $2\pi^*$ states ~3 eV above the doped Au Fermi level (**Figure 2*b***). The spread of these states increases in the presence of dopants via strong hybridization of the N_2 $2\pi^*$ with occupied dopant *d* orbitals. Likewise, the N_2 1π states just below the Fermi level can back-donate into empty dopant *d* orbitals (75). Thus, these DFT simulations suggest CT as a viable mechanism for H_2 desorption and N_2 dissociation enhancements on Pd(111) and *M*-doped Au(111) surfaces, respectively. In Section 4, however, we present excited-state calculations for these systems (Section 4.2.1 for Pd–H_2 and Section 4.2.2 for Au–*M*–N_2) that show RET and not CT is the more likely primary mechanism for plasmon-enhanced reaction rates in these cases. This highlights the danger

in interpreting ground-state, DFT-derived electronic properties, as it can lead to incorrect qualitative and quantitative conclusions regarding the role of surface plasmons in catalysis.

4. THE THERMODYNAMICS AND KINETICS OF PLASMONIC CATALYSIS FROM MULTIREFERENCE WAVEFUNCTION THEORIES

4.1. Density Functional Embedding Theory and Embedded Correlated Wavefunction Theory

Methods based on correlated wavefunction (CW) approaches include the correct physics for CT and other electronic transitions. Unfortunately, their high computational cost and unfavorable scaling become prohibitive for large systems. An accuracy-retaining solution is to split the system into different subsystems, e.g., the important catalytic center that requires a high-accuracy treatment and the remainder of the catalyst crystal, also referred to as the environment, that can be treated at a lower level of theory, and use embedding techniques to account for the interaction between them (**Figure 3a**) (76). One such embedding method is density functional embedding theory (DFET). In DFET (77, 78), an exact unique embedding potential is determined from DFT. The embedding potential is subsequently applied in subsystem calculations to incorporate the effects of the subsystem interactions. The first step in DFET is to determine the embedding potential to represent the interaction of the catalytically active center with its environment at the level of periodic DFT calculations (**Figure 3a,b**) (79). Embedded CW (ECW) and DFT calculations, with the embedding potential added to the Hamiltonian (80), then are performed on the cluster representing the catalytically active center, and regionally corrected periodic DFT energies are obtained according to

$$E^{emb} = E_{slab}^{DFT} + \left(E_{emb-cluster}^{CW} - E_{emb-cluster}^{DFT} \right).$$

The total embedded energy, E^{emb}, is obtained by correcting the DFT energy from a periodic slab calculation of the total system, E_{slab}^{DFT}, with the difference between embedded CW, $E_{emb-cluster}^{CW}$, and embedded DFT, $E_{emb-cluster}^{DFT}$, cluster calculations. CW methods express the many-body wavefunction as a linear combination of ground- and excited-state Slater determinants constructed from a set of orthonormal spin-orbitals. CW methods include single-reference configuration interaction (CI) singles (CIS) and CI singles and doubles (CISD) (81), multireference singles and doubles CI (81, 82), complete active space self-consistent field (CASSCF) (83–85), and coupled-cluster singles and doubles (CCSD) with higher excitation extensions (86). For example, in CASSCF, a single-state (SS) or state-averaged (SA) energy is minimized variationally with respect to the weights of the (symmetry-adapted) Slater determinants of the different electronic configurations and the coefficients of the basis functions used to expand the orbitals (**Figure 3c**). The electronic configurations are defined within a user-defined space consisting of highly correlated or chemically relevant orbitals. Perturbative corrections usually accompany multiconfigurational schemes to reduce the optimization space; these include the complete active space second-order perturbation theory (CASPT2) (87, 88), n-electron valence second-order perturbation theory (NEVPT2) (89), and CCSD with perturbative triples (90), among others. In the bodies of work discussed in Section 4.2, DFET combined with ECW is used to obtain PESs of surface reactions for both corrected ground states and excited states (91). We note that this method was also used recently not for plasmonic photocatalysis but to explain chemical interface Landau damping in Au nanorods via molecularly induced dipoles that serve as scattering centers (92). Henceforth, for any methods that combine DFET with ECW, the CW method will be prefixed with emb-.
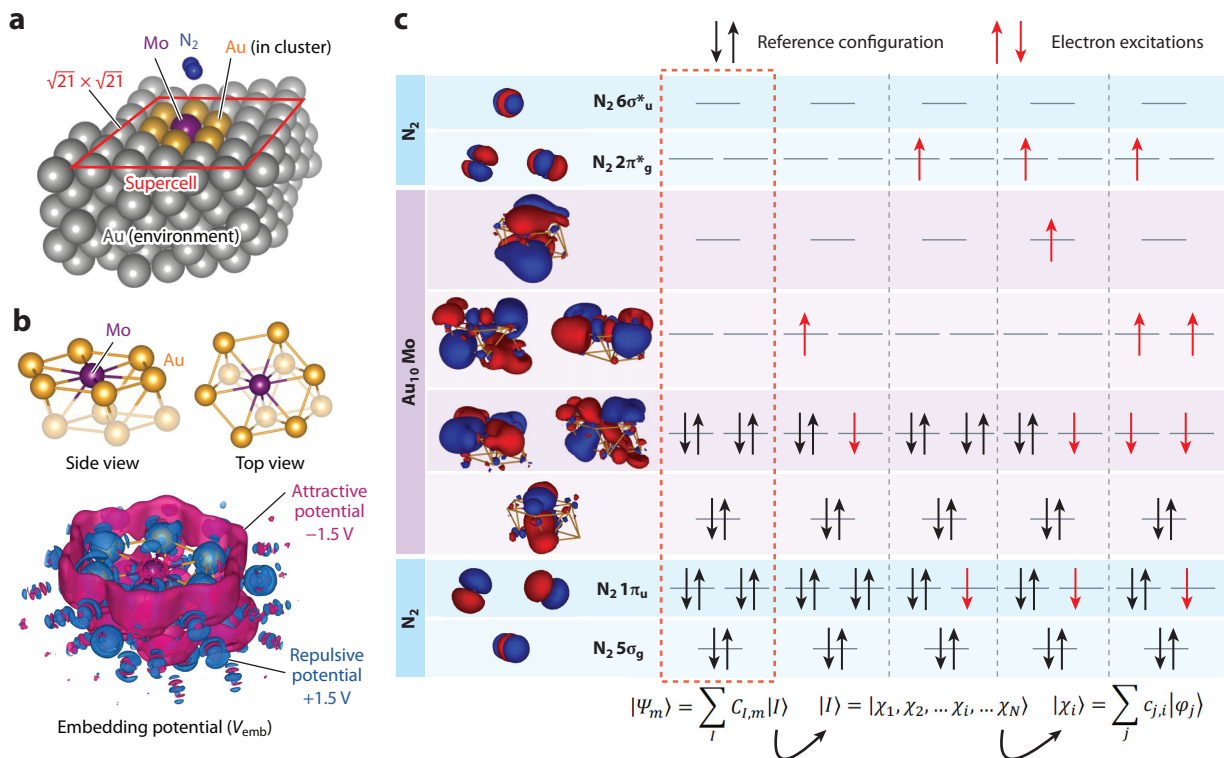
Figure 3

(*a*) An illustration showing a $(\sqrt{21} \times \sqrt{21})$ $R10.9°$ five-layer Mo-substituted Au(111) periodic slab with the supercell outlined in red. The cluster and environment are predefined to be used in the ensuing density functional embedding theory (DFET) calculation to determine the optimized embedding potential. (*b, top*) The $Au_{10}Mo$ cluster carved out from the slab in panel *a* (subsurface atoms are faded out). (*Bottom*) A representation of an isosurface of the embedding potential generated for the environment and cluster fragments described in panel *a* and the top of panel *b* (attractive potential, *purple*; repulsive potential, *blue*). Panels *a* and *b* adapted from Reference 54; copyright 2017 American Association for the Advancement of Science (AAAS). (*c, left*) Illustrations showing the ground-state embedded complete active space self-consistent field (emb-CASSCF) natural orbitals for the $Au_{10}Mo$ embedded-cluster model with N_2 ~5 Å away from the surface. The N_2 and cluster-derived orbitals (combinations of Au 6*s* and Mo 4*d* orbitals) are labeled. Phases of the orbitals are shown in red and blue; isosurface value equals ±0.02 atomic units. The left part of panel *c* adapted from Reference 54; copyright 2017 AAAS. (*Right*) In CASSCF, a variationally optimized sum of all possible electronic configurations ($|I\rangle$) within the active space is used to expand the many-electron wavefunction (Ψ_m) of state *m* (ground or excited state). $|I\rangle$ is either, depending on the code used, a Slater determinant or a spin-symmetry-adapted Slater determinant known as a configuration state function, which is composed of antisymmetrized products of spatial orbitals $|\chi i\rangle$ and spin eigenfunctions. The $|\chi_i\rangle$ are expanded in an atomic-orbital basis $|\varphi_j\rangle$. The coefficients in front of $|I\rangle$ and $|\varphi_j\rangle$, $C_{I,m}$ and $c_{j,i}$, are optimized by minimizing the total energy or state-averaged (SA) total energy (for SA-CASSCF). A mixture of initially occupied and empty orbitals (*horizontal lines* with *black up* and *down arrows* representing up- and down-spin electrons) comprises the active space (in *red dashed line box*). For example, for a system with an even number of electrons, the singlet electronic ground state may have a dominant configuration in which each occupied orbital has a pair of up- and down-spin electrons. The electronic configurations are generated from this dominant ground-state configuration (in *red dashed line box*) by a series of single- or multiple-electron excitations (*red up* and *down arrows*).

4.2. Examples Using Density Functional Embedding Theory and Embedded Correlated Wavefunction Theory

Among the reactions studied for LSPR activation (see Section 1.2) thus far, the breakdown or synthesis of small molecules is the most suitable to which to apply ECW theory because of the lower computational costs to model them and the simpler mechanistic pathways involved. In the

following subsections, recent examples of the utility of ECW theory to predict and understand the behavior of plasmon-induced dissociation and desorption of H_2, decomposition of N_2 and NH_3, and activation of methane and fluorinated methane are presented.

4.2.1. H_2 dissociation and molecular desorption.

Mukherjee et al. (9) used emb-CIS to understand how illuminated Au NPs could split hydrogen when Au itself is inert. Their predicted ground-state MEP for H_2 dissociative adsorption on Au(111) begins with gas-phase H_2 molecules weakly physisorbing on bridge sites. Then the H–H bond stretches, eventually reaching a transition-state structure with a dissociation barrier of ~2.3 eV [using emb-Hartree-Fock (emb-HF) for the ground state]. As illustrated in **Figure 4a**, at the ground-state minimum, if the system absorbs ~1.8 eV energy from an LSPR, then hot electrons can populate the Feshbach resonance in a transient $H_2^{\delta-}$, which weakens the H–H bond (9). Via population of an LSPR-accessible excited state, Mukherjee et al. (9) predicted the excited-state barrier decreases by ~0.6 eV relative to the ground-state one, explaining the observed HD production enhancement. Subsequent emb-CASPT2 calculations by Libisch et al. (10) predicted the ground-state H_2 dissociation barrier on Au(111) to be much lower, ~1.2 eV versus the earlier emb-HF estimate of ~2.3 eV [later corrected to 1.9 eV (10)]. No emb-CASPT2 excited-state barriers were predicted, however. **Figure 4b** displays the ground-state (emb-HF) and the sixth and seventh excited-state (emb-CIS) PESs, exhibiting barrier reduction in two excited states (10). Moreover, although CT during excitation was hypothesized in the original work (9), later ECW calculations (10) do not support this hypothesis, based on a CW-derived atomic charge analysis. The barrier reduction instead can be explained by PI-RET (Section 2.3) to populate excited states with lower barriers (10). A similar study was performed on Al NPs by Zhou et al. (11). **Figure 4c** shows that excess negative charge concentrates outside the (physisorbed) H_2 bond on Al(111), as the H_2 antibonding orbital is partially occupied. Identifying clear excited-state reaction pathways was difficult because of the dense distribution of low-lying Al(111) surface states due to its nearly free-electron character (11); however, that dense distribution implies that numerous nonadiabatic transitions may facilitate excited-state barrier crossing.

As discussed in Section 1.3, the reactivity of Pd for catalytic H_2 production can be substantially enhanced by coupling Pd NPs as the reactor with Al NPs as the antenna (27). The PESs for H_2 associative desorption on Pd(111), as constructed by Spata & Carter (93) via emb-NEVPT2, are displayed in **Figure 4d**. The lowest-energy adsorption sites are the fcc sites. The rate-determining step for H_2 desorption on Pd is the migration of one of the H atoms from the fcc site to around the hcp site (int-1), with a ground-state barrier of ~0.8 eV. The system can absorb ~1 eV energy from an LSPR and experience an excited-state barrier of only ~0.1 eV, followed by deexcitation to the ground state at int-1. A second excitation of ~1.4 eV results in a second barrier of ~0.3 eV to overcome, following the excited-state manifold. Finally, the researchers conclude that a reduction in the overall activation energy of ~0.5 eV is achievable upon excitation, leading to faster H_2 (or HD) production via these excitation-deexcitation processes. No CT state is involved. Note that the overall desorption process requires at least two electronic transitions (**Figure 4d**). This suggests a superlinear dependence of the rate on the number of incident photons per unit time (Section 2.4). Indeed, the HD production rate on Al-Pd NPs was observed to depend superlinearly on laser power (27).

4.2.2. N_2 activation.

The Haber-Bosch process, which is used for industrial ammonia synthesis, reacts $N_2(g)$ with $H_2(g)$ at energy-intensive high temperatures (~500°C) and pressures (~200 atm), despite the reaction being thermodynamically favorable under ambient conditions (94). N_2 dissociation is the primary kinetic bottleneck (95). Via DFT-PBE-D3BJ calculations,
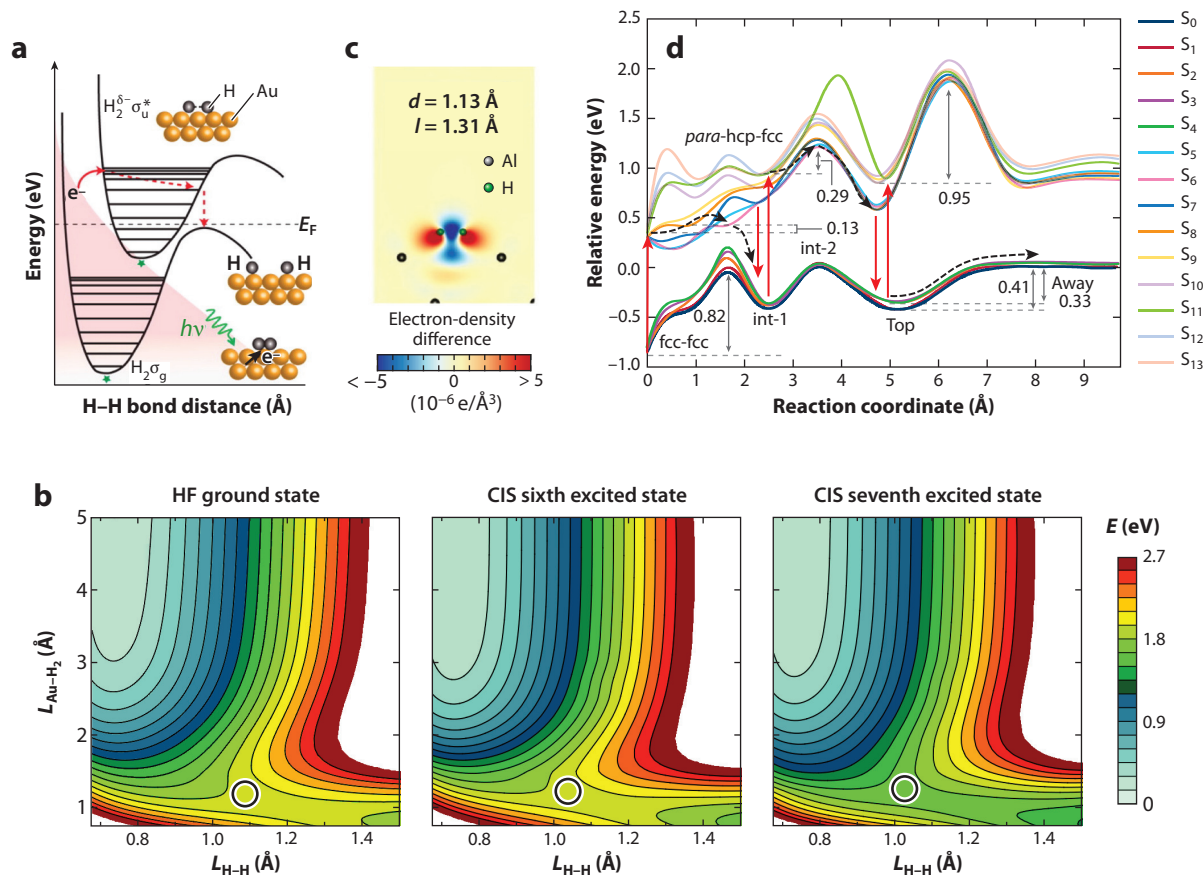
Figure 4

H_2 dissociative adsorption on Au and Al as well as H_2 associative desorption from Pd. (*a*) Proposed CT mechanism of hot-carrier-induced H_2 dissociative adsorption on Au NPs. Panel *a* adapted from Reference 9; copyright 2013 American Chemical Society. (*b*) PESs for H_2 dissociation on Au(111) via hcp-fcc adsorption. (*Left* to *right*) The HF ground state and the sixth and seventh excited states from emb-CIS are depicted here; the excited states show reduced activation barriers toward dissociation compared to that of the ground state. Black circles mark the approximate positions of the transition states. Panel *b* adapted from Reference 10; copyright 2016 De Gruyter. (*c*) Electron-density differences for H_2 (with H–H distance $l = 1.31$ Å and the H_2–Al top layer distance $d = 1.13$ Å) before and after being adsorbed on Al(111). Panel *c* adapted from Reference 11; copyright 2016 American Chemical Society. (*d*) emb-NEVPT2 ground- (S_0) and excited-state (S_1–S_{13}) PESs along the reaction coordinate for H_2 associative desorption from Pd(111). Vertical red arrows represent excitations and deexcitations. Curved dashed black arrows represent the productive pathways that involve both ground and excited states, while the barrier heights are marked by double-headed gray arrows. Panel *d* adapted from Reference 93; copyright 2018 American Chemical Society. Abbreviations: CT, charge transfer; emb-CIS, embedded configuration interaction singles; emb-NEVPT2, *n*-electron valence second-order perturbation theory; fcc, face-centered cubic; hcp, hexagonal close-packed; int-1 and int-2, intermediates 1 and 2; HF, Hartree-Fock; NP, nanoparticle; PES, potential energy surface.

Martirez & Carter (75) explored the best dopants to enhance N_2 binding to Au. They found Fe and Mo to be most promising for N_2 binding among the dopants evaluated, i.e., Fe, Co, Ni, and Mo, each of which binds N_2 favorably in its respective pure form (75). AuMo(111) was also predicted to exhibit Ru(111)-like high activity (54). The same researchers then identified Mo-surface-doped Au NPs as being able to activate N_2 using NIR to Vis light, owing to Mo's excellent N_2 activation and Au's LSPR. Structures along the DFT-PBE-D3BJ MEP and the emb-NEVPT2 ground- and
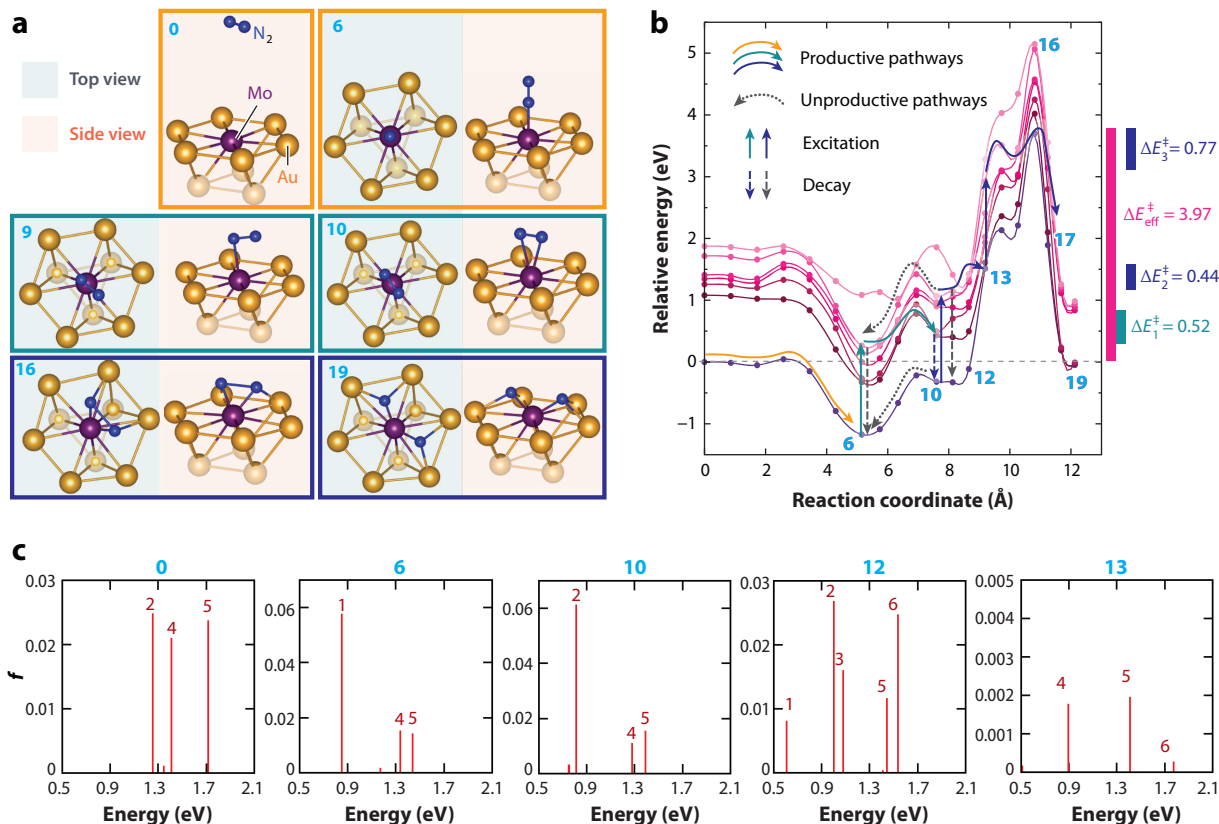
Figure 5

(*a*) Representations that show periodic DFT-PBE-D3BJ structures along the MEP for N_2 dissociation (only the Au_9Mo fragments are shown for clarity). Orange boxes: reactant and product (structures 0 and 6) of N_2 adsorption (vertically oriented) on Mo; green boxes: transition state and product of rotation of the adsorbed N_2 from vertical to horizontal orientation (structures 9 and 10); blue boxes: transition state and product of the dissociation of the horizontally oriented adsorbed N_2 to two N atoms adsorbed on adjacent hollow sites (structures 16 and 19). Top and side views of the structures are shown except for structure 0. These structures correspond to the numerically marked (*blue numbers*) points in the plot in panel *b*, as labeled. (*b*) Representations of emb-NEVPT2 ground- and excited-energy curves for the spin singlet state showing up to the sixth excited state. Different color intensity is assigned for each curve (*dark* to *light*: low to high energy). Possible lower-barrier trajectories are marked with arrows (*orange*, *green*, and *blue*). These trajectories involve the structures in panel *a* in boxes with their corresponding colors. Ground- and excited-state effective thermal barriers ($\Delta E_n^{\ddagger}$, $n = 1, 2,$ and 3 for steps 1, 2, and 3, which involve excited states, and the overall ground-state effective barrier, $n = $ eff) are shown on the right margin in eV/N_2. The bars mark the range over which the barrier heights were measured. (*c*) Absorption spectra (oscillator strength, *f*, versus excitation energy) are shown for select structures along the dissociation trajectory in panel *a*, calculated from emb-SA-CASSCF transition dipole moments and emb-NEVPT2 excitation energies. Excited-state indices are given at the top of each red vertical line (*red numbers*). The structure indices (*blue numbers*) on top of each panel correspond to the same structures shown in panel *a* and marked in panel *b*. Abbreviations: D3BJ, D3 method with Becke-Johnson damping; DFT, density functional theory; emb-NEVPT2, embedded *n*-electron valence second-order perturbation theory; emb-SA-CASSCF, embedded state-averaged complete active space self-consistent field theory; MEP, minimum energy path; PBE, Perdew-Burke-Ernzerhof approximation. Figure adapted with permission from Reference 54; copyright 2017 American Association for the Advancement of Science.

excited-state energies along that MEP are shown in **Figure 5a** and **5b**, respectively. A series of excitations requiring energies of only ~1.5 eV (NIR to Vis) enables the low-barrier dissociation of N_2. The largest effective barrier was calculated to be only 0.77 eV (**Figure 5b**), reasonable to overcome at relatively mild temperatures, making these NPs promising as a low-temperature

Haber-Bosch catalyst under illumination (54). The researchers also calculated the oscillator strengths of the excited states from emb-SA-CASSCF for each structure along the MEP (**Figure 5c**), which can correlate with their lifetimes (96) and FRET rate (Section 2.3). As in the case of H_2 (Section 4.2.1), no significant CT state is found for N_2 adsorbed on either Fe- or Mo-doped Au for excitation energies up to ~2 eV (54, 97), suggesting that energy transfer is dominated by FRET here as well. Moreover, the simulations suggest the need for multiple electronic transitions to overcome the high kinetic barrier, a behavior known to persist for dissociating diatomic molecules (Section 2.4) (27, 58, 59).

Beyond providing mechanistic insight, these results also allow us to reach a practical conclusion. Coupling illuminated surface-Mo-doped Au NPs' ability to break the N_2 bond and illuminated pure Au NPs' ability to break the H_2 bond under relatively mild conditions, which suggests a possible path toward sustainable ammonia synthesis, given that N–H bond formation should require less energy input compared to breaking these very strong bonds in the reactants.

4.2.3. NH₃ decomposition. NH_3 can be used as a potential H_2 storage medium; thus, its decomposition catalyzed by plasmonic metallic NPs is worth exploring. Experimentally, Ru-doped Cu NPs (24, 25) exhibit an N_2 production rate in the dark that is zeroth order with respect to NH_3; under light illumination, the reaction switches to almost first order in NH_3. Emb-CASPT2 calculations were used to explain the change in kinetics. **Figure 6a** and **6b** displays emb-CASPT2 PESs computed by Bao & Carter (98) for the bottleneck steps on Ru-doped Cu(111), namely the first N–H bond scission in NH_3 and the associative desorption of N_2, respectively. NH_3 interacts strongly with Ru, with a heat of adsorption of approximately −1.3 eV. By comparison, the exothermicity of NH_3 adsorption on pure Cu(111) is only approximately −0.8 eV (99). The ground-state
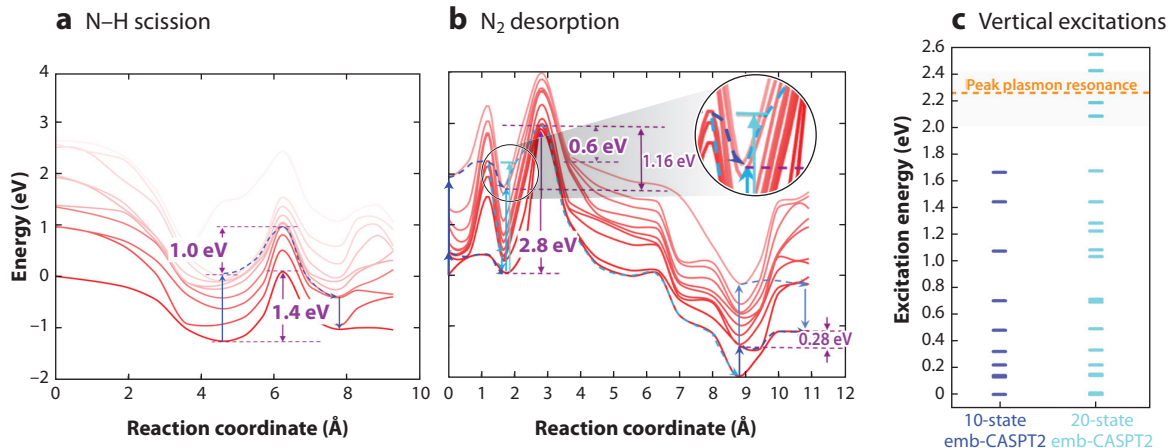

a N–H scission **b** N_2 desorption **c** Vertical excitations

Figure 6

Embedded correlated wavefunction theory predictions for key steps in NH_3 decomposition on Ru-doped Cu(111). (*a*) Graph showing embedded complete active space second-order perturbation theory (emb-CASPT2) ground- and excited-state potential energy surfaces (PESs) along the reduced reaction coordinate for $NH_3(g) \rightarrow NH_2(ad) + H(ad)$. (*b*) Graph showing emb-CASPT2 ground- and excited-state PESs along the reduced reaction coordinate for $2N(ad) \rightarrow N_2(g)$. For panels *a* and *b*, a different color intensity is assigned for each curve (*red* to *pink*: low to high energy) and curved arrows represent the productive (thermal) pathways, while barrier heights are indicated by double-headed arrows. Vertical arrows represent excitations and deexcitations. The large inset circle shows a magnified view of the smaller circle around 2 Å along the reaction coordinate. (*c*) Plot showing vertical excitation energies for the chemisorbed two-nitrogen-atom (2N) structure at the reaction coordinate ~2 Å as calculated by 10-state and 20-state emb-CASPT2. Figure adapted with permission from Reference 101; copyright 2019 American Chemical Society.

barriers for Ru-doped Cu(111) are ~1.4 eV for N–H bond scission and ~2.8 eV for N_2 desorption. Thus, under thermocatalytic conditions, the overall reaction rate for N_2 production is determined by N_2 associative desorption, which is independent of NH_3 pressure, consistent with experiment (98). Upon illumination, N–H bond scission (**Figure 6a**) starting from the adsorbed NH_3 minimum energy structure (at reaction coordinate $s \sim 4.6$ Å) can proceed via absorption of ~1.3 eV energy from an LSPR and promotion to the eighth excited state. Due to the small energy gaps between low-lying states, reactive trajectories can easily transition nonadiabatically to the third excited state around the transition state structure ($s \sim 6.2$ Å), leading to an effective excited-state barrier of ~1.0 eV (**Figure 6a**). Note that a large gap (~1.4 eV) exists between the eighth and ninth adsorbate-metal excited states. The excitation energy required to pump the system from the ground state to above the ninth excited state exceeds the peak of the LSPR for Ru-doped Cu NPs (~2.25 eV). Therefore, higher excited states are not accessible at the peak energy and the barrier for this N–H bond scission cannot decrease further. In contrast, for the chemisorbed two-nitrogen-atom (2N) structure (**Figure 6b**), the high-lying states are accessible via an LSPR. The researchers verified this by computing vertical excitation energies at $s \sim 2$ Å at the emb-CASPT2 level with 10 and 20 states (**Figure 6c**). The system can absorb ~2.2 eV of energy, leading to an excited-state barrier of ~0.6 eV (**Figure 6b**). Thus, the emb-CASPT2 calculations explain why the rate-determining step switches from nitrogen associative desorption to N–H bond scission under illumination (98), which qualitatively explains the observed first-order reaction kinetics (24, 25).

4.2.4. C–H and C–F bond activation.

Syngas, which is primarily composed of CO and H_2, is a feedstock for industrial-scale chemical production (100–102). Natural gas (such as CH_4) produces syngas by steam reforming, partial oxidation with O_2, or dry reforming with CO_2 (100–102). Methane dry reforming (MDR) is a highly endothermic and endergonic ($\Delta H° = 247.3$ and $\Delta G° = 170.8$ kJ/mol CH_4 at 298 K) process (103) and is kinetically hindered even in the presence of metal catalysts, thus requiring high operating temperatures (900–1,300 K) (100). Zhou et al. (26) explored low-temperature plasmon-mediated MDR on Ru-doped Cu (CuRu) NPs for MDR (**Figure 7a**). These researchers mapped out chemical pathways for the key MDR step of CH_4 decomposition, on both pure and Ru-doped Cu surfaces, using DFT-PBE-D3BJ with CI-NEB. The more accurate emb-NEVPT2 was then used to obtain both ground- and excited-state energy curves. In the ground state, replacing even one Cu with an Ru atom lowered the barrier for both rate-limiting dehydrogenation steps, from 2.51 eV to 0.70 eV for CH_4 and from 1.94 eV to 1.10 eV for CH dehydrogenation (see **Figure 7b** for the latter step on CuRu) (26). Excited-state channels with decreased dissociation barriers accessible at ~1.4 eV photon energy are available for CuRu(111) (the barrier decreases from 1.10 to 0.4 eV) (**Figure 7b**), while pure Cu(111) cannot access such a mechanism. Experiments showed that pure Cu NPs lack activity and selectivity even with light illumination. Coking (C deposition) is also prevalent in the dark, even with Ru. The role of Ru was therefore found to be crucial in (*a*) catalyzing C–H activation, (*b*) arresting coke formation (due to the immobilization of surface C species at Ru), and (*c*) funneling energy onto the molecule (26).

The efficient activation of C(sp^3)–F bonds under mild conditions is difficult due to their large bond dissociation energies. Robatjazi et al. (104) demonstrated that hydrodefluorination can be realized efficiently via $CH_3F(g) + D_2(g) \rightarrow CH_3D(g) + DF(g)$ on Al–Pd antenna–reactors under illumination. Emb-CASPT2 calculations on Pd(111) from the same researchers predict that, in the ground state, the rate-determining C–F bond cleavage step has a barrier of ~1.1 eV, while subsequent C–D bond formation requires at least ~0.8 eV energy to overcome the thermal barrier. The researchers also concluded that the surface coverage of D atoms, which consume the active sites on Pd, plays an indispensable role in controlling the overall kinetics due to the small
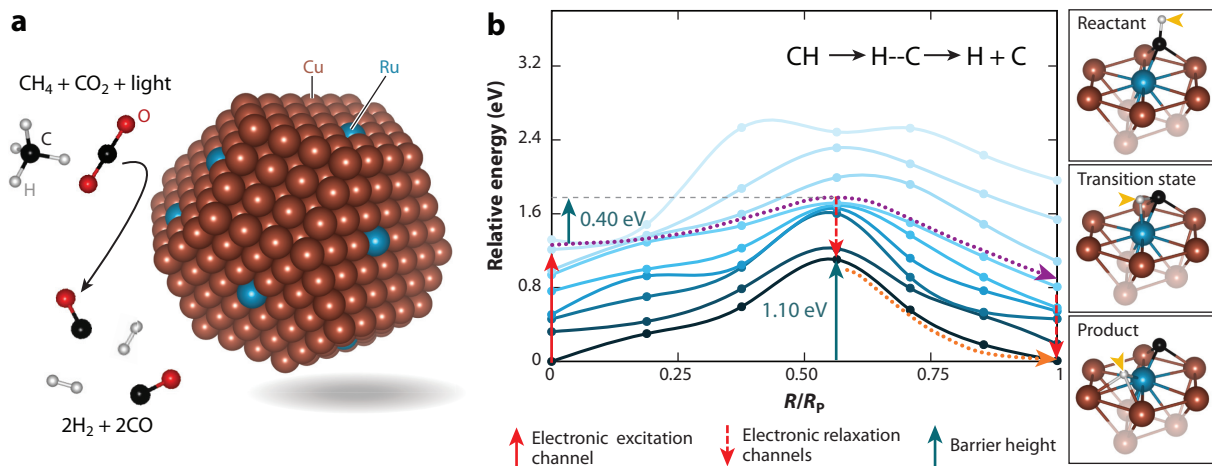
Figure 7

(*a*) Illustration showing an Ru-single-atom-substituted Cu surface alloy NP catalyst with dry reforming reactants and products. (*b*, *left*) Ground- and excited-state energy curves for C–H activation on CuRu(111) from emb-NEVPT2, shown with different color intensities (*dark* to *light*: low to high energy). Possible electronic excitation and relaxation channels (*vertical red arrows*) are shown. In addition, possible trajectories involving both excited-state (*purple dotted line* as a visual guide) and ground-state (*orange dotted line*) curves are marked. The ground-state and effective excited-state barriers are also shown. MEP structures are taken from ground-state DFT-PBE-D3BJ with CI-NEB calculations. R/R_P refers to the reduced reaction coordinate along the MEP. (*Right*) The structures of (*top*) the reactant, (*middle*) the transition state, and (*bottom*) the product are shown here. Only the Cu_6Ru and a shaded sublayer Cu_3 slab fragment are shown for clarity. Yellow arrowheads mark the detaching H. Abbreviations: CI-NEB, climbing-image nudged elastic band; D3BJ, D3 method with Becke-Johnson damping; DFT, density functional theory; emb-NEVPT2, embedded *n*-electron valence second-order perturbation theory; MEP, minimum energy path; NP, nanoparticle; PBE, Perdew-Burke-Ernzerhof approximation. Figure adapted from Reference 26; copyright 2020 Nature Publishing Group.

dissociative adsorption energy of D_2 on Pd. Under light illumination, these emb-CASPT2 calculations reveal that transitions from the ground to the ninth excited state at chemisorbed minima enable substantial reductions in barriers. Specifically, the excited-state barriers become $\sim$0.2 eV for CH_3F dissociative adsorption, $\sim$0.3 eV for CH_3D associative desorption, and $\sim$0.3 eV for D_2 associative desorption. Given that the expected level of uncertainty in predicted energetics is $\sim$0.1 eV, the researchers predict that under illumination, D_2 desorption competes effectively with CH_3F dissociative adsorption and CH_3D associative desorption in determining the excited-state kinetics.

5. SUMMARY AND OUTLOOK

In principle, a diverse set of quantum mechanics methods can be used to understand and predict plasmon-based heterogeneous catalysis. DFT has been an invaluable tool in the field of thermal heterogeneous catalysis and so furnishes a basis for comparison. However, DFT's ability to predict excited-state properties, let alone excited-state surface reactions, is questionable because of the errors inherent in approximate XC functionals. Many ab initio correlated wavefunction methods can aid experiments in understanding light-driven chemical processes. The field of plasmonic catalysis notably demands such methods while modeling surface chemistry. This is a tall order, given the size of acceptable models to simulate a surface. DFET is a tool that enables the use of multiconfigurational ab initio methods in the context of plasmonic catalysis. Here, we have not considered the utility of time-dependent DFT, which has been used to characterize optoelectronic

and plasmonic properties of metal clusters and NPs. Possible avenues of future exploration are the use of time-dependent DFT (with, e.g., range-separated XC functionals) in modeling LSPRs and chemical reactions concurrently and establishing correlations of ground-state DFT electronic and structural properties with excited-state CW-derived properties to accelerate the discovery of catalytically appropriate combinations of plasmonically active metals and reactions.

DISCLOSURE STATEMENT

The authors are not aware of any affiliations, memberships, funding, or financial holdings that might be perceived as affecting the objectivity of this review.

ACKNOWLEDGMENTS

LITERATURE CITED

1. Kelly KL, Coronado E, Zhao LL, Schatz GC. 2003. The optical properties of metal nanoparticles: the influence of size, shape, and dielectric environment. *J. Phys. Chem. B* 107:668–77
2. Blaber MG, Arnold MD, Ford MJ. 2010. A review of the optical properties of alloys and intermetallics for plasmonics. *J. Phys. Condens. Matter* 22:143201
3. McClain MJ, Schlather AE, Ringe E, King NS, Liu LF, et al. 2015. Aluminum nanocrystals. *Nano Lett.* 15:2751–55
4. Link S, El-Sayed MA. 1999. Spectral properties and relaxation dynamics of surface plasmon electronic oscillations in gold and silver nanodots and nanorods. *J. Phys. Chem. B* 103:8410–26
5. Biggins JS, Yazdi S, Ringe E. 2018. Magnesium nanoparticle plasmonics. *Nano Lett.* 18:3752–58
6. Moskovits M. 1985. Surface-enhanced spectroscopy. *Rev. Mod. Phys.* 57:783–826
7. Moskovits M. 2013. Persistent misconceptions regarding SERS. *Phys. Chem. Chem. Phys.* 15:5301–11
8. Web Sci. 2020. *Web of Knowledge*. Clarivate Analytics, Philadelphia, PA, accessed May 24, 2020. **https://apps.webofknowledge.com**
9. Mukherjee S, Libisch F, Large N, Neumann O, Brown LV, et al. 2013. Hot electrons do the impossible: plasmon-induced dissociation of H_2 on Au. *Nano Lett.* 13:240–47
10. Libisch F, Cheng J, Carter EA. 2013. Electron-transfer-induced dissociation of H_2 on gold nanoparticles: excited-state potential energy surfaces *via* embedded correlated wavefunction theory. *Z. Phys. Chem.* 227:1455–66. Corrigendum. 2016. *Z. Phys. Chem.* 230:131–32
11. Zhou L, Zhang C, McClain MJ, Manavacas A, Krauter CM, et al. 2016. Aluminum nanocrystals as a plasmonic photocatalyst for hydrogen dissociation. *Nano Lett.* 16:1478–84
12. Christopher P, Xin HL, Linic S. 2011. Visible-light-enhanced catalytic oxidation reactions on plasmonic silver nanostructures. *Nat. Chem.* 3:467–72
13. Zhang X, Li XQ, Zhang D, Su NQ, Yang WT, et al. 2017. Product selectivity in plasmonic photocatalysis for carbon dioxide hydrogenation. *Nat. Commun.* 8:14542
14. Xiao Q, Sarina S, Bo AX, Jia JF, Liu HW, et al. 2014. Visible light-driven cross-coupling reactions at lower temperatures using a photocatalyst of palladium and gold alloy nanoparticles. *ACS Catal.* 4:1725–34
15. Yu SJ, Wilson AJ, Heo J, Jain PK. 2018. Plasmonic control of multi-electron transfer and C–C coupling in visible-light-driven CO_2 reduction on Au nanoparticles. *Nano Lett.* 18:2189–94

16. Ferrando R, Jellinek J, Johnston RL. 2008. Nanoalloys: from theory to applications of alloy clusters and nanoparticles. *Chem. Rev.* 108:845–910

17. Yi CY, Dongare PD, Su MN, Wang WX, Chakraborty D, et al. 2017. Vibrational coupling in plasmonic molecules. *PNAS* 114:11621–26

18. Yorulmaz M, Hoggard A, Zhao HQ, Wen FF, Chang WS, et al. 2016. Absorption spectroscopy of an individual Fano cluster. *Nano Lett.* 16:6497–503

19. King NS, Liu LF, Yang X, Cerjan B, Everitt HO, et al. 2015. Fano resonant aluminum nanoclusters for plasmonic colorimetric sensing. *ACS Nano* 9:10628–36

20. Amendola V, Scaramuzza S, Agnoli S, Polizzi S, Meneghetti M. 2014. Strong dependence of surface plasmon resonance and surface enhanced Raman scattering on the composition of Au–Fe nanoalloys. *Nanoscale* 6:1423–33

21. Alexander DTL, Forrer D, Ross E, Lidorikis E, Agnoli S, et al. 2019. Electronic structure-dependent surface plasmon resonance in single Au–Fe nanoalloys. *Nano Lett.* 19:5754–61

22. Cable RE, Schaak RE. 2007. Solution synthesis of nanocrystalline M–Zn (M = Pd, Au, Cu) intermetallic compounds via chemical conversion of metal nanoparticle precursors. *Chem. Mater.* 19:4098–104

23. Sarina S, Zhu HY, Jaatinen E, Xiao Q, Liu HW, et al. 2013. Enhancing catalytic performance of palladium in gold and palladium alloy nanoparticles for organic synthesis reactions through visible light irradiation at ambient temperatures. *J. Am. Chem. Soc.* 135:5793–801

24. Zhou L, Swearer DF, Robatjazi H, Alabastri A, Christopher P, et al. 2018. Quantifying hot carrier and thermal contributions in plasmonic photocatalysis. *Science* 362:69–72

25. Zhou LA, Swearer DF, Robatjazi H, Alabastri A, Christopher P, et al. 2019. Response to comment on "Quantifying hot carrier and thermal contributions in plasmonic photocatalysis." *Science* 364:eaaw9545

26. Zhou L, Martirez JMP, Finzel J, Zhang C, Swearer DF, et al. 2020. Light-driven methane dry reforming with single atomic site antenna-reactor plasmonic photocatalysts. *Nat. Energy* 5:61–70

27. Swearer DF, Zhao H, Zhou L, Zhang C, Robatjazi H, et al. 2016. Heterometallic antenna–reactor complexes for photocatalysis. *PNAS* 113:8916–20

28. Aslam U, Chavez S, Linic S. 2017. Controlling energy flow in multimetallic nanostructures for plasmonic catalysis. *Nat. Nanotechnol.* 12:1000–5

29. Wang L, Clavero C, Huba Z, Carroll KJ, Carpenter EE, et al. 2011. Plasmonics and enhanced magneto-optics in core-shell Co-Ag nanoparticles. *Nano Lett.* 11:1237–40

30. Zheng ZK, Tachikawa T, Majima T. 2015. Plasmon-enhanced formic acid dehydrogenation using anisotropic Pd–Au nanorods studied at the single-particle level. *J. Am. Chem. Soc.* 137:948–57

31. Wang F, Li CH, Chen HJ, Jiang RB, Sun LD, et al. 2013. Plasmonic harvesting of light energy for Suzuki coupling reactions. *J. Am. Chem. Soc.* 135:5588–601

32. Swearer DF, Leary RK, Newell R, Yazdi S, Robatjazi H, et al. 2017. Transition-metal decorated aluminum nanocrystals. *ACS Nano* 11:10281–88

33. Swearer DF, Robatjazi H, Martirez JMP, Zhang M, Zhou L, et al. 2019. Plasmonic photocatalysis of nitrous oxide into N_2 and O_2 using aluminum–iridium antenna–reactor nanoparticles. *ACS Nano* 13:8076–86

34. Rej S, Mascaretti L, Santiago EY, Tomanec O, Kment S, et al. 2020. Determining plasmonic hot electrons and photothermal effects during H_2 evolution with TiN–Pt nanohybrids. *ACS Catal.* 10:5261–71

35. Cortie MB, McDonagh AM. 2011. Synthesis and optical properties of hybrid and alloy plasmonic nanoparticles. *Chem. Rev.* 111:3713–35

36. Link S, El-Sayed MA. 2003. Optical properties and ultrafast dynamics of metallic nanocrystals. *Annu. Rev. Phys. Chem.* 54:331–66

37. Brongersma ML, Halas NJ, Nordlander P. 2015. Plasmon-induced hot carrier science and technology. *Nat. Nanotechnol.* 10:25–34

38. Narang P, Sundararaman R, Atwater HA. 2016. Plasmonic hot carrier dynamics in solid-state and chemical systems for energy conversion. *Nanophotonics* 5:96–111

39. Morton SM, Silverstein DW, Jensen L. 2011. Theoretical studies of plasmonics using electronic structure methods. *Chem. Rev.* 111:3962–94

40. Moskovits M. 2015. The case for plasmon-derived hot carrier devices. *Nat. Nanotechnol.* 10:6–8

41. Deleted in proof

42. Christopher P, Xin HL, Marimuthu A, Linic S. 2012. Singular characteristics and unique chemical bond activation mechanisms of photocatalytic reactions on plasmonic nanostructures. *Nat. Mater.* 11:1044–50

43. Manjavacas A, Liu JG, Kulkarni V, Nordlander P. 2014. Plasmon-induced hot carriers in metallic nanoparticles. *ACS Nano* 8:7630–38

44. Sundararaman R, Narang P, Jermyn AS, Goddard WA III, Atwater HA. 2014. Theoretical predictions for hot-carrier generation from surface plasmon decay. *Nat. Commun.* 5:5788

45. Zheng BY, Zhao HQ, Manjavacas A, McClain M, Nordlander P, Halas NJ. 2015. Distinguishing between plasmon-induced and photoexcited carriers in a device geometry. *Nat. Commun.* 6:7797

46. Tolk NH, Traum MM, Tully JC, Madey TE, eds. 1982. *Desorption Induced by Electronic Transitions DIET I: Proceedings of the First International Workshop*, *Williamsburg, Virginia, USA, May 12–14*. Berlin: Springer

47. Misewich JA, Heinz TF, Newns DM. 1992. Desorption induced by multiple electronic transitions. *Phys. Rev. Lett.* 68:3737–40

48. Watanabe K, Menzel D, Nilius N, Freund HJ. 2006. Photochemistry on metal nanoparticles. *Chem. Rev.* 106:4301–20

49. Frischkorn C, Wolf M. 2006. Femtochemistry at metal surfaces: nonadiabatic reaction dynamics. *Chem. Rev.* 106:4207–33

50. Jain PK. 2019. Taking the heat off of plasmonic chemistry. *J. Phys. Chem. C* 123:24347–51

51. Adleman JR, Boyd DA, Goodwin DG, Psaltis D. 2009. Heterogenous catalysis mediated by plasmon heating. *Nano Lett.* 9:4417–23

52. Cushing SK, Li JT, Meng FK, Senty TR, Suri S, et al. 2012. Photocatalytic activity enhanced by plasmonic resonant energy transfer from metal to semiconductor. *J. Am. Chem. Soc.* 134:15033–41

53. Hsu L-Y, Ding W, Schatz GC. 2017. Plasmon-coupled resonance energy transfer. *J. Phys. Chem. Lett.* 8:2357–67

54. Martirez JMP, Carter EA. 2017. Prediction of a low-temperature N_2 dissociation catalyst exploiting near-IR–to–visible light nanoplasmonics. *Sci. Adv.* 3:eaao4710

55. Scholes GD. 2003. Long-range resonance energy transfer in molecular systems. *Annu. Rev. Phys. Chem.* 54:57–87

56. Kim Y, Torres DD, Jain PK. 2016. Activation energies of plasmonic catalysts. *Nano Lett.* 16:3399–407

57. Seemala B, Therrien AJ, Lou M, Li K, Finzel JP, et al. 2019. Plasmon-mediated catalytic O_2 dissociation on Ag nanostructures: hot electrons or near fields? *ACS Energy Lett.* 4:1803–9

58. Linic S, Aslam U, Boerigter C, Morabito M. 2015. Photochemical transformations on plasmonic metal nanoparticles. *Nat. Mater.* 14:567–76

59. Zhang X, Li XQ, Reish ME, Zhang D, Su NQ, et al. 2018. Plasmon-enhanced catalysis: distinguishing thermal and nonthermal effects. *Nano Lett.* 18:1714–23

60. Bredas J-L. 2014. Mind the gap! *Mater. Horiz.* 1:17–19

61. Cohen AJ, Mori-Sánchez P, Yang W. 2008. Insights into current limitations of density functional theory. *Science* 321:792–94

62. Kohn W, Sham LJ. 1965. Self-consistent equations including exchange and correlation effects. *Phys. Rev.* 140:1133

63. Perdew JP, Burke K, Ernzerhof M. 1996. Generalized gradient approximation made simple. *Phys. Rev. Lett.* 77:3865–68

64. Hammer B, Hansen LB, Nørskov JK. 1999. Improved adsorption energetics within density-functional theory using revised Perdew-Burke-Ernzerhof functionals. *Phys. Rev. B* 59:7413–21

65. Becke AD, Johnson ER. 2005. A density-functional model of the dispersion interaction. *J. Chem. Phys.* 123:154101

66. Tkatchenko A, Scheffler M. 2009. Accurate molecular van der Waals interactions from ground-state electron density and free-atom reference data. *Phys. Rev. Lett.* 102:073005

67. Lee K, Murray ED, Kong LZ, Lundqvist BI, Langreth DC. 2010. Higher-accuracy van der Waals density functional. *Phys. Rev. B* 82:081101

68. Grimme S, Antony J, Ehrlich S, Krieg H. 2010. A consistent and accurate *ab initio* parametrization of density functional dispersion correction (DFT-D) for the 94 elements H-Pu. *J. Chem. Phys.* 132:154104

69. Grimme S, Ehrlich S, Goerigk L. 2011. Effect of the damping function in dispersion corrected density functional theory. *J. Comput. Chem.* 32:1456–65

70. Steinmann SN, Corminboeuf C. 2011. A generalized-gradient approximation exchange hole model for dispersion coefficients. *J. Chem. Phys.* 134:044117

71. Truhlar DG. 2019. Dispersion forces: neither fluctuating nor dispersing. *J. Chem. Educ.* 96:1671–75

72. Sheppard D, Terrell R, Henkelman G. 2008. Optimization methods for finding minimum energy paths. *J. Chem. Phys.* 128:134106

73. Henkelman G, Uberuaga BP, Jonsson H. 2000. A climbing image nudged elastic band method for finding saddle points and minimum energy paths. *J. Chem. Phys.* 113:9901–4

74. Dronskowski R, Blochl PE. 1993. Crystal orbital Hamilton populations (COHP): energy-resolved visualization of chemical bonding in solids based on density-functional calculations. *J. Phys. Chem.* 97:8617–24

75. Martirez JMP, Carter EA. 2016. Thermodynamic constraints in using AuM (M = Fe, Co, Ni, and Mo) alloys as N_2 dissociation catalysts: functionalizing a plasmon-active metal. *ACS Nano* 10:2940–49

76. Huang P, Carter EA. 2008. Advances in correlated electronic structure methods for solids, surfaces, and nanostructures. *Annu. Rev. Phys. Chem.* 59:261–90

77. Huang C, Pavone M, Carter EA. 2011. Quantum mechanical embedding theory based on a unique embedding potential. *J. Chem. Phys.* 134:154110

78. Yu K, Libisch F, Carter EA. 2015. Implementation of density functional embedding theory within the projector-augmented-wave method and applications to semiconductor defect states. *J. Chem. Phys.* 143:102806

79. Yu K, Krauter CM, Dieterich JM, Carter EA. 2017. Density and potential functional embedding: theory and practice. In *Fragmentation: Toward Accurate Calculations on Complex Molecular Systems*, ed. MS Gordon, pp. 81–111. Hoboken, NJ: John Wiley & Sons

80. Krauter CM, Carter EA. 2017. Embedding integral generator. *GitHub*. **https://github.com/EACcodes/EmbeddingIntegralGenerator**

81. Sherrill CD, Schaefer HF. 1999. The configuration interaction method: advances in highly correlated approaches. *Adv. Quantum Chem.* 34:143–269

82. Roos BO, Siegbahn PEM. 1980. Direct CI method with a multiconfigurational reference state. *Int. J. Quantum Chem.* 17:485–500

83. Roos BO. 1980. The complete active space SCF method in a fock-matrix-based super-CI formulation. *Int. J. Quantum Chem.* 18:175–89

84. Roos BO, Taylor PR, Siegbahn PEM. 1980. A complete active space SCF method (CASSCF) using a density matrix formulated super-CI approach. *Chem. Phys.* 48:157–73

85. Siegbahn PEM, Almlöf J, Heiberg A, Roos BO. 1981. The complete active space SCF (CASSCF) method in a Newton–Raphson formulation with application to the HNO molecule. *J. Chem. Phys.* 74:2384–96

86. Helgaker T, Jørgensen P, Olsen J. 2000. *Molecular Electronic-Structure Theory*. Chichester, UK: John Wiley & Sons

87. Andersson K, Malmqvist PA, Roos BO, Sadlej AJ, Wolinski K. 1990. Second-order perturbation theory with a CASSCF reference function. *J. Phys. Chem.* 94:5483–88

88. Andersson K, Malmqvist PA, Roos BO. 1992. Second-order perturbation theory with a complete active space self-consistent field reference function. *J. Chem. Phys.* 96:1218–26

89. Angeli C, Cimiraglia R, Evangelisti S, Leininger T, Malrieu JP. 2001. Introduction of *n*-electron valence states for multireference perturbation theory. *J. Chem. Phys.* 114:10252–64

90. Raghavachari K, Trucks GW, Pople JA, Head-Gordon M. 1989. A fifth-order perturbation comparison of electron correlation theories. *Chem. Phys. Lett.* 157:479–83

91. Libisch F, Huang C, Carter EA. 2014. Embedded correlated wavefunction schemes: theory and applications. *Acc. Chem. Res.* 47:2768–75

92. Foerster B, Spata VA, Carter EA, Sönnichsen C, Link S. 2019. Plasmon damping depends on the chemical nature of the nanoparticle interface. *Sci. Adv.* 5:eaav074

93. Spata VA, Carter EA. 2018. Mechanistic insights into photocatalyzed hydrogen desorption from palladium surfaces assisted by localized surface plasmon resonances. *ACS Nano* 12:3512–22

94. Appl M. 2000. Ammonia, 2. Production processes. In *Ullmann's Encyclopedia of Industrial Chemistry*, ed. F Ullmann, M Bohnet, pp. 139–225. Weinheim, Ger.: Wiley-VCH

95. Kandemir T, Schuster ME, Senyshyn A, Behrens M, Schlogl R. 2013. The Haber-Bosch process revisited: on the real structure and stability of "ammonia iron" under working conditions. *Angew. Chem. Int. Ed.* 52:12723–26

96. Turro NJ. 1991. *Modern Molecular Photochemistry*. Sausalito, CA: Univ. Sci. Books

97. Martirez JMP, Carter EA. 2017. Excited-state N_2 dissociation pathway on Fe-functionalized Au. *J. Am. Chem. Soc.* 139:4390–98

98. Bao JL, Carter EA. 2019. Rationalizing the hot-carrier-mediated reaction mechanisms and kinetics for ammonia decomposition on ruthenium-doped copper nanoparticles. *J. Am. Chem. Soc.* 141:13320–23

99. Bao JL, Carter EA. 2019. Surface-plasmon-induced ammonia decomposition on copper: excited-state reaction pathways revealed by embedded correlated wavefunction theory. *ACS Nano* 13:9944–57

100. Aramouni NAK, Touma JG, Abu Tarboush B, Zeaiter J, Ahmad MN. 2018. Catalyst design for dry reforming of methane: analysis review. *Renew. Sustain. Energy Rev.* 82:2570–85

101. Pakhare D, Spivey J. 2014. A review of dry (CO_2) reforming of methane over noble metal catalysts. *Chem. Soc. Rev.* 43:7813–37

102. Hickman DA, Schmidt LD. 1993. Production of syngas by direct catalytic oxidation of methane. *Science* 259:343–46

103. Chase MW, Davies CA, Downey JR, Frurip DJ, McDonald RA, Syverud AN. 1986. *NIST JANAF Thermochemical Tables 1985*. Gaithersburg, MD: Natl. Inst. Stand. Technol.

104. Robatjazi H, Bao JL, Zhou L, Zhang M, Christopher P, et al. 2020. Plasmon-driven carbon-fluorine (C(sp^3)-F) bond activation with mechanistic insights into hot-carrier-mediated pathways. *Nat. Catal.* 3:564–73